Deep Autofocus for Synthetic Aperture Sonar

Isaac D. Gerg and Vishal Monga

***Abstract*—Synthetic aperture sonar (SAS) requires precise positional and environmental information to produce well-focused output during the image reconstruction step. However, errors in these measurements are commonly present resulting in defocused imagery. To overcome these issues, an *autofocus* algorithm is employed as a post-processing step after image reconstruction for the purpose of improving image quality using the image content itself. These algorithms are usually iterative and metric-based in that they seek to optimize an image sharpness metric. In this letter, we demonstrate the potential of machine learning, specifically deep learning, to address the autofocus problem. We formulate the problem as a self-supervised, phase error estimation task using a deep network we call Deep Autofocus. Our formulation has the advantages of being non-iterative (and thus fast) and not requiring ground truth focused-defocused images pairs as often required by other deblurring deep learning methods. We compare our technique against a set of common sharpness metrics optimized using gradient descent over a real-world dataset. Our results demonstrate Deep Autofocus can produce imagery that is perceptually as good as benchmark iterative techniques but at a substantially lower computational cost. We conclude that our proposed Deep Autofocus can provide a more favorable cost-quality trade-off than state-of-the-art alternatives with significant potential of future research.**

I. Introduction

Autofocus is a family of algorithms usually employed after the image reconstruction step with the purpose of improving image sharpness resulting from mis-estimation of platform/environmental parameters during the motion estimation procedure. It usually uses the image content itself as a reference by which to improve perceived image sharpness. Fig.1 shows an example image and output of the procedure. Usually, these methods operate iteratively making adjustments to phase across the aperture to optimize a sharpness metric. Two examples of commonly used metrics are maximization of image contrast [1] and minimization of image entropy [2].

Metric-based autofocus schemes usually follow a common pattern [3]. First, a model of the global phase error is specified. This is often a polynomial [1]. Next, an initial guess of the global phase error is applied to the image. This guess can be bootstrapped from optimization of previous images. After that, the sharpness metric is measured on the image along with the gradient with respect to the phase error estimate. Finally, an optimization step is performed which ingests this information and proposes a new global phase error to examine. The method then repeats until convergence is met.

Broadly speaking, metric-based autofocus algorithms suffer from three classes of problems:

1) Compute speed. Many autofocus algorithms are iterative and often need several iterations for convergence. Each iteration can be expensive requiring several fast Fourier transforms (FFTs) [1], [4] or even echo backprojection (BP) [5].
2) Sensitivity to tuning parameters. For the iterative optimization methods, the associated step size and stopping criteria must be articulated usually at the trade-off between convergence speed, image quality, and environmental robustness. Also, some methods require the identification of *scene scatterers* [6], [7] and/or *peak-picking* [8], [9] during intermediate steps. In the former, the problem is ill-posed and often corrected through the use of heuristic outlier detection. In the latter, system specific heuristics are usually employed such as limiting the region where the peak can be detected. In all cases, the signal model cannot be robustly specified so hand-tuned heuristics are employed.
3) The definition of image sharpness is ill-posed. Methods optimize over a specified image quality metric but no metric is universally robust. Commonly used metrics are prone to getting trapped in local minima [10] and they operate on a single image at time; each image is autofocused independently of the rest. Becoming trapped in a local minimum often manifests in an image where one bright scatterer is incorrectly *over-focused* at the expense of defocusing the rest of the scene.

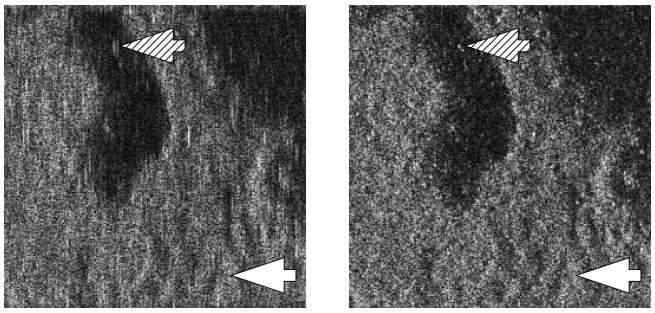

(a) Original Defocused Image (b) Deep Autofocus Result

Fig. 1: (a) Example SAS image with quadratic phase error due to mis-estimation of sound speed and/or vehicle along-track velocity. (b) Corrected image using our proposed Deep Autofocus method. The striped arrow points to a point-scatterer which should be well focused but is blurred in the along-track direction due to error. The solid arrow shows bottom texture with reduced fidelity due to error. Some autofocus methods rely on the ability to identify point-scatters in the defocused image to work. As we can see from (a) the identification of defocused point-scatters can be quite difficult when phase error is great.

We motivate the application of deep learning techniques to the autofocus problem to address the aforementioned issues. Specifically, **we propose a method called Deep Autofocus with the following properties**:

1) While there is general interest in applying deep learning methods to various parts of synthetic aperture radar (SAR) processing [11], **to the best of our knowledge,**

This work was supported by Office of Naval Research under grants N00014-19-1-2638, N00014-19-1-2513.

I. D. Gerg is with the Applied Research Laboratory and School of EECS at the Pennsylvania State University. V. Monga is with the School of EECS at the Pennsylvania State University (http://signal.ee.psu.edu).

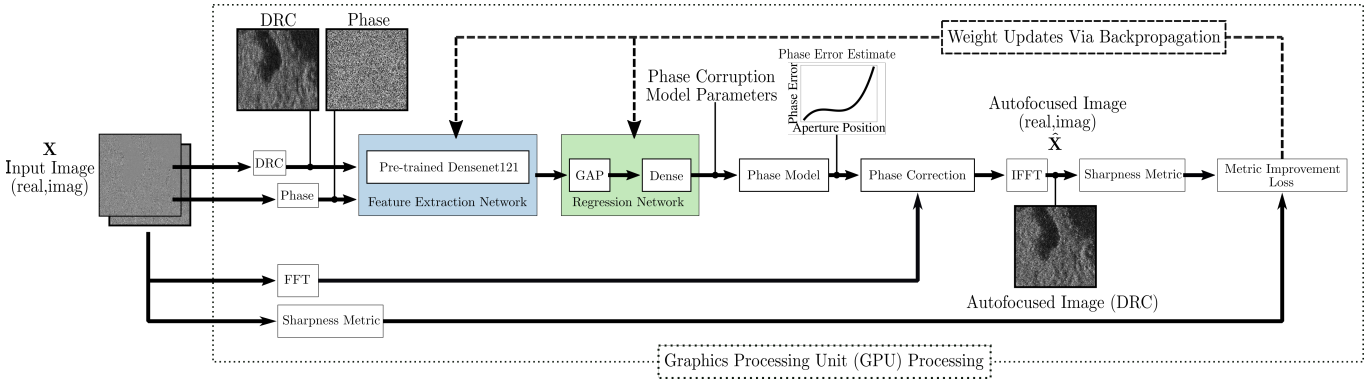

Fig. 2: Our proposed Deep Autofocus architecture. The network inputs a single-look complex (SLC) image, $\mathbf{x}$, which is dynamic range compressed (DRC) and passed into a feature extraction network (blue) along with the SLC's phase. The features are then fed to a regression network (green) which outputs the phase corruption model parameters, which in this case are the coefficients of ten-degree polynomial modeling the phase error. The phase error is then applied in the Fourier domain, computed by the fast Fourier transform (FFT), of the SLC and then inverse Fourier transformed back to the spatial domain. Finally, the relative increase in contrast between the input and output images magnitude images is measured and weights are backpropagated to maximize this quantity. Our formulation is end-to-end differentiable and trained on a GPU.

this is the first use of deep learning for the SAS autofocus problem. By nature of deep learning, our algorithm is fast (it runs on graphics processing units – GPUs) and is non-iterative. Our formulation lends itself naturally to autofocusing groups of images in parallel.

2) **Forgoes the onerous tasks of creating hand-crafted and data-driven scatterer detection and peak-picking algorithms required as steps in many existing autofocus algorithms.** Through the use of human visual system priors built into convolution neural networks (CNNs), robust scene interpretation is automatically learned as part of the autofocusing task.
3) **Applies knowledge gained from autofocusing one image to all images.** Our method learns on batches of images at time, so autofocus *rules* learned for one image must be also work well on others.

Autofocus is the last step in a lengthy SAS image reconstruction pipeline. Many of the steps in this pipeline require robust estimation models and would likely benefit from the good results deep learning exhibits especially where such models cannot be exactly specified [12]. This work incorporates deep learning in a final stage of the image reconstruction pipeline, autofocus. In the future, perhaps other portions of the SAS image reconstruction pipeline will see improvements from the use of deep learning.

II. Proposed Method Deep Autofocus

Our formulation is inspired the work of [13]. Their efforts demonstrate that humans can easily identify and classify motion estimation errors in SAS imagery simply by visual inspection. This *scene interpretation* skill is easy accomplished by sonar analysts but difficult to specify analytically. This work is the first to utilize convolutional neural networks [14], [15] to tackle the SAS autofocus problem.

We formulate the problem in a similar approach as [1]. In this approach, an image sharpness metric is defined along with its derivative with respect to a global phase correction applied in the Fourier domain. A solution is found using simple gradient descent (GD). Likewise, our formulation explicitly computes and applies a global phase correction in the Fourier domain but with two important differences. The first difference is that we use a feature extraction network and a regression network to estimate the phase correction model parameters instead of iteration. The second difference is we learn the feature extraction and regression network weights by operating on batches of images using stochastic gradient descent (SGD) method instead of GD.

Similar to [4] and [1], we model the phase error as a polynomial. In these works, they show results for a 6th order polynomial. In this work, we used a 10th order polynomial simply because its larger than previous works giving merit to our approach. The parameters of this polynomial are estimated by the regression network. We forgo estimating the zero-th and first-order coefficients because the former infers no change to the image content and the latter simply translates it; neither modify the image content in a meaningful way.

Fig.2 depicts the network architecture of Deep Autofocus. The input is a single-look complex (SLC) image in real and imaginary representation. The image is then dynamic range compressed (DRC) using the rational tone mapping operator of [16] and it, along with the SLC phase, are fed to a pre-trained Densenet121 network which is our feature extraction network (blue). Global average pooling (GAP) is applied to the feature embedding and the result fed to multi-layer fully connected network serving as our regression network (green) which outputs the phase error parameters for our phase error correction (PEC) model. The PEC is then applied to the Fourier transform (azimuth direction) of the SLC and then inverse Fourier transformed back to the spatial domain. Finally, the intensity of the resultant image is formed and its relative sharpness improvement with respect to the input SLC is measured; it is this self-supervised loss which relieves the need for ground truth well-focused images. Our formulation is completely differentiable (this includes the FFT/IFFT, sharpness metric, and dynamic range compression) allowing end-to-training through backpropagation.

The weights of the networks are modified through back-

Table I: Data partitioning used in Deep Autofocus for training, validation, and testing.

Purpose	Number of Images	Notes
Training	120	Data augmentation used (phase error of random polynomials of both degree and coefficients)
Validation	360	120 original images, 120 positive QPE, 120 negative QPE (see Eq (2))
Test	792	264 original images, 264 positive QPE, 264 negative QPE

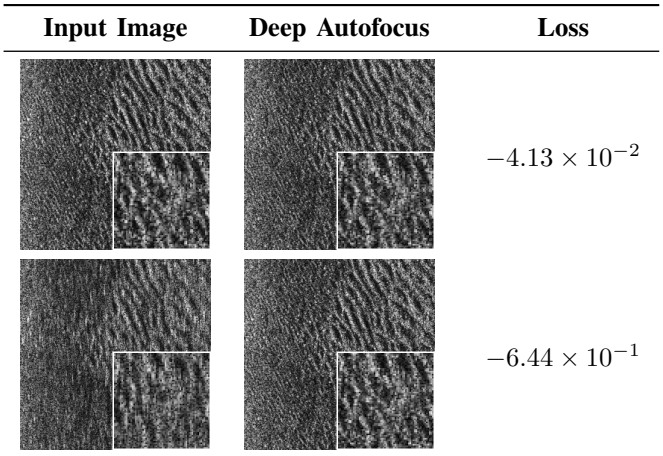

Fig. 3: Example behavior of our loss function, (1). The top row of images shows a mostly focused input image which was able to be slightly improved using our method. The input/output pair yield the corresponding negative loss close to zero since the image was mostly focused initially. The bottom row of images show a poorly focused input image which was able to be significantly improved using our method. The input/output pair yield a much larger negative loss since the initial image was defocused.

propagation of the self-supervised loss of (1).

$$\mathcal{L}(\mathbf{x}) = -\left(\frac{\mathcal{M}_{\text{MNS}}(\|\hat{\mathbf{x}}\|) - \mathcal{M}_{\text{MNS}}(\|\mathbf{x}\|)}{\mathcal{M}_{\text{MNS}}(\|\mathbf{x}\|)}\right) \tag{1}$$

where $\mathbf{x}$ is the input SLC, $\hat{\mathbf{x}}$ is the phase corrected SLC, and $\mathcal{M}_{\text{MNS}}$ is the mean normalized stddev metric defined in Table II. We chose this sharpness metric over the others because it gave the best overall performance among the metrics in Fig.4. **The merits of the cost function in (1)**:The training loss function we employ in (1) has some noteworthy properties. It is positive when image sharpness, as deemed by the metric, is reduced. It is zero when there is no change in image sharpness. And, it is negative when image sharpness is improved. Fig.3 shows an example of the loss' behavior.

Deep Autofocus tries to find solutions which make (1) as negative of possible for each image. Common loss functions in deep learning usually seek to drive their loss function to zero for all input data/label pairs. In the autofocus problem, optimal solutions for each image do not exist at the same level set. For example, one optimally focused image may have a minimum at -1.2 and another may have a minimum at -30.3. In other words, there is no absolute sharpness metric. We use the relative metric improvements instead of the metric itself as a loss because we found empirically that training directly with the sharpness metric performs sub-optimally.

III. Experiments and Results

A. Dataset Description

The images used in training and evaluation of Deep Autofocus is described in Table I and are collected from an experimental high-frequency SAS system. The images were reconstructed using an ω-k algorithm. Some of the images appear to have residual focus errors but nothing catastrophic. For the validation and test sets, we artificially corrupt the images with quadratic phase error to evaluate robustness. This error is applied in the Fourier domain along the azimuthal axis by,

$$\phi(p, \alpha) = \alpha p^2 \tag{2}$$

where p is the azimuthal aperture position normalized to $[-1, 1]$ and α is the error strength in radians. We augment the original images from the test and validations sets with QPE where we set $\alpha \pm 12$ radians.

For the validation and tests sets, we choose the magnitude of α so that the QPE is severe demonstrating the ability of our method, but also important, we create corruptions with opposite signs (i.e α is positive and α is negative). The is motivated by examining the point spread function (PSF) of QPE. In [13], we see that the PSF for QPE is symmetric about the azimuth axis. This implies that two images corrupted with the same QPE magnitude but with different signs are indistinguishable to a human. This motivates the need to input SLC phase in Fig.2 which resolves this ambiguity. We verified this by creating a network which forgoes phase input and saw that the performance noticeably suffers.

B. Deep Autofocus Training Procedure

We train Deep Autofocus using SGD with a batch size of thirty-two and a learning rate of 10^{-1}. Training halts at 10,000 epochs and the model with the best validation performance is used for analysis on the test set. Data augmentation is used during training by artificially adding polynomial phase error to the input SLC's. We do this by first selecting the order of the polynomial from integer set $\{2, 3, 4, 5, 6, 7, 8, 9, 10\}$. Next we select the coefficients randomly from $U \sim [-1, 1]$. After that, we normalize the coefficients so that the maximum magnitude value of the polynomial evaluated at $x = \pm 1$ is 1.0. Finally, we scale the resultant function by $U \sim [-18, 18]$.

C. Comparison to Existing Sharpness Metrics

For comparison, we evaluate Deep Autofocus against four common sharpness metrics. For each metric and image, we optimize using gradient descent and the loss form of (1). Each gradient descent runs for ten iterations. The learning rate for gradient descent is selected from the one giving the best mean results from the set of learning rates $\{10^{-6}, 10^{-5}, 10^{-4}, 10^{-3}, 10^{-2}, 10^{-1}, 10^{0}, 10^{1}, 10^{2}, 10^{3}\}$ over the image set. To facilitate compute performance comparisons between Deep Autofocus and the comparison metrics, we implement the gradient descent optimization of each metric on the same GPU used to train Deep Autofocus and also use analytic gradients. All methods were implemented using Tensorflow 2.1 [18].

Obtaining ground-truth, absolute focused images from a real-world SAS is difficult. Human inspection cannot be relied on to determine if an image is absolutely well focused because residual focus error may be present in the SLC which is not

Table II: List of image sharpness metrics used in this work for comparison to Deep Autofocus. $g(x, y)$ is the input single look complex (SLC) image. We make $b = \epsilon$ in OSF as it was shown when b is large the metric is equivalent to SSI.

Source	Metric Name	Equation	Desired Extremum
Fienup [1] (2000)	Sum of Squared Intensity (SSI)	$\mathcal{M}_{\text{SSI}} = \sum_x \sum_y \lvert g(x,y)\rvert^4$	Maximum
Fortune, et al. [3] (2001)	Mean Normalized Stddev (MNS)	$\mathcal{M}_{\text{MNS}} = \frac{\text{stddev}(\lvert g(x,y)\rvert)}{\text{mean}(\lvert g(x,y)\rvert)}$	Maximum
Schulz [17] (2006)	Optimal Sharpness Function (OSF)	$\mathcal{M}_{\text{OSF}} = \sum_x \sum_y -\ln(\lvert g(x,y)\rvert^2 + b)$	Minimum
Zeng, et al. [2] (2013)	Minimum Entropy (ME)	$\mathcal{M}_{\text{ME}} = -\sum_x \sum_y \lvert g(x,y)\rvert^2 \ln(\lvert g(x,y)\rvert^2)$	Minimum

evident in the dynamic range compressed (DRC) image. Also, some images cannot be autofocused using a global correction because of spatially varying sound speed or bathymetry in the image. Finally, simulation could be used but is very expensive build and run. Together, these issues make it difficult to define "ground-truth" when assessing autofocus efficacy.

We address the aforementioned issues through two means:

1) We create comparison images by optimizing for sharpness using the best non-deep-learning metric from Table II, $\mathcal{M}_{\text{MNS}}$ [3], and optimize the images using a sophisticated optimizer, Nelder-Mead of Scipy [19]. We call these images the *benchmark* images. The optimizer is allowed to run for hundreds of iterations taking several hours to process the test set. We acknowledge in practice this is an impractical configuration, but we employ it here for the purposes of creating our benchmark optimized images.
2) We assess the efficacy of each method by comparing it to the benchmark images using several perceptually oriented quality measures. Because slight differences in the phase correction can result in drastically different realizations of the speckle noise, we despeckle the images prior to evaluation. Despeckling is done using the total variation method of [20], [21].

D. Results on Real-World SAS Imagery

Fig.4 shows the results of measuring image similarity between Deep Autofocus using several perceptual image similarity measures [26]. Table III compares the run-time between the iterative metrics and Deep Autofocus. We see that Deep Autofocus produces imagery which is perceptually similar to the benchmark images but at almost two orders of magnitude less time. Additionally, we see that our method is able to disambiguate the QPE sign of Eq. 2 through the use of the phase. Recall, if we forgo the network input of SLC phase, our formulation does not work as well. It is remarkable that the network is able to discern information from the phase map given its discontinuous (e.g. phase wrap) and random nature [27], [28], especially since no man-made objects are present in the dataset (man-made objects often yield structure in the phase domain due to their specular acoustic return). This is in line with the recent results of [29] where they describe a simple deep neural network with the ability to unscramble XOR'ed imagery which is also highly discontinuous. Finally, Fig.5 shows an image and phase error correction comparison for one of the images with the lowest SSIM of the reconstructed to the benchmark.

We give a visual comparison of the best and worst Deep Autofocus images with respect to the SSIM metric in the supplementary material.

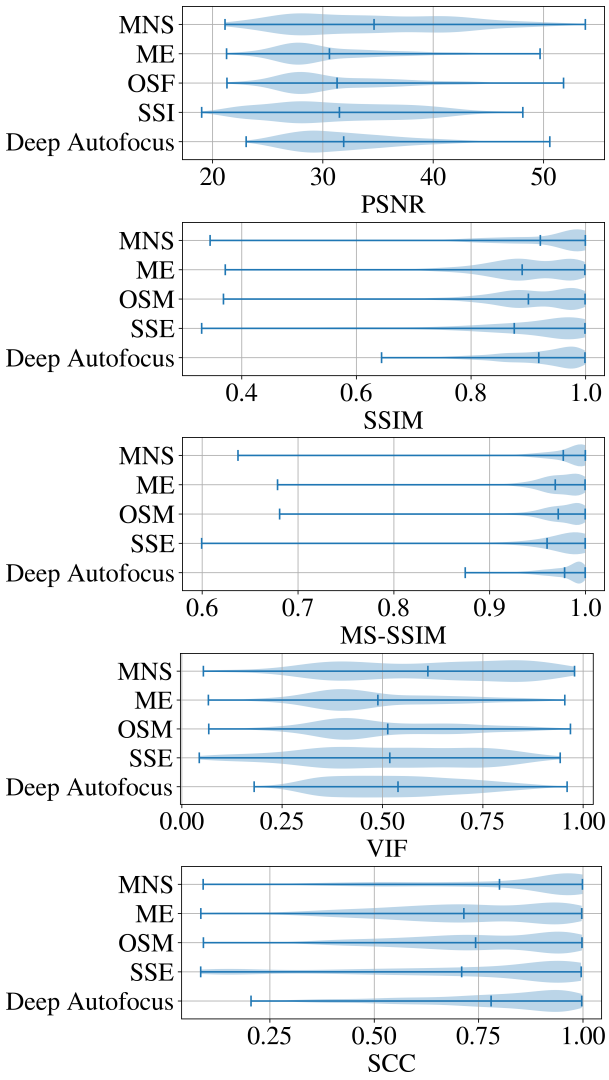

Fig. 4: We compare the Deep Autofocus images to the benchmark images using several perceptual-oriented measures. The images are despeckled using [20], [21] before making the comparison. For all measures, higher values indicated more similarity to the benchmark images. The measures evaluated are peak signal-to-noise ratio (PSNR) [22], structural similarity metric (SSIM) [22], multiscale SSIM (MS-SSIM) [23], visual information fidelity (VIF) [24], and spatial correlation coefficient (SCC) [25].

IV. Conclusion

Autofocus methods for SAS are difficult to deploy in real-time environment because of their compute requirements and brittleness if one gets unlucky scene content. It was shown by [13] that humans can identify and classify SAS motion estimation errors by imagery alone. To this end, we propose a machine learning, specifically deep learning, method to tackle the autofocus problem. We demonstrate that a simple

Table III: Run-time performance of each class of algorithm. These values were computed by measuring the time it takes to process the test set and then dividing by the number of samples in the test set. Lower numbers indicate faster run-time. Note, large run-times are not suitable for use in unmanned underwater vehicles (UUVs) where computation power is limited. All metrics optimized using gradient descent exhibit similar run-time. Deep Autofocus and GD methods were run on the same GPU; the Benchmark was run on a CPU using the Scipy optimize library.

Algorithm	Iterations	Mean Runtime [s]
SSI-GD	10	1.1×10^{0}
MNS-GD	10	1.1×10^{0}
OSF-GD	10	1.1×10^{0}
ME-GD	10	1.1×10^{0}
Benchmark	≈ 2300	5×10^{2}
Deep Autofocus	1	1.8×10^{-2}

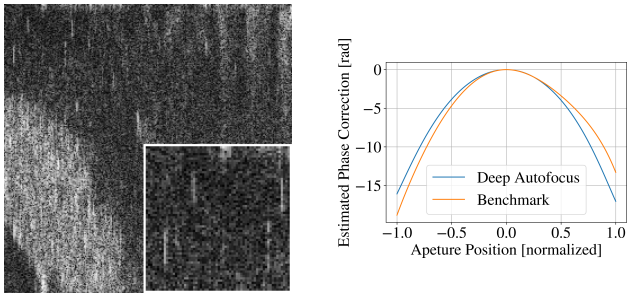

(a) Input Image (b) Phase Correction

(c) Benchmark (d) Deep Autofocus

Fig. 5: Comparison of Deep Autofocus and benchmark autofocusing results. (a) is the original, defocused image. (b) shows the phase corrected estimated by both methods. (c) and (d) show the autofocused results. We see from (b), (c), and (d) that Deep Autofocus results in an image that with focus quality on par with the benchmark images. This SSIM between (c) and (d) was in the worst five of the test set demonstrating that despite low a SSIM score, our method produced a well-focused image.

CNN design can autofocus imagery just as good as current techniques but with a much reduced compute burden.

Future research in the area could include the incorporation of spatially-heterogeneous phase error from locally varying wave propagation speeds or bathymetry (a formulation similar to [30] is a natural starting point), and the creation of a human-based perpetual metric akin to LPIPS [15] but for SAS image sharpness. We are encouraged by the success of this work and should ground truth imagery come available (e.g. simulation), deep learning can use the ground truth to likely exceed current benchmarks, while maintaining computational benefits.

V. Acknowledgment

The authors thank NSWC - Panama City Division for providing the data used in this experiment.

References

[1] J. Fienup, "Synthetic-aperture radar autofocus by maximizing sharpness," *Optics Letters*, vol. 25, no. 4, pp. 221–223, 2000.
[2] T. Zeng *et al.*, "SAR image autofocus utilizing minimum-entropy criterion," *IEEE GRSL*, vol. 10, no. 6, pp. 1552–1556, 2013.
[3] S. Fortune *et al.*, "Statistical autofocus of synthetic aperture sonar images using image contrast optimisation," in *IEEE OCEANS*, vol. 1, 2001, pp. 163–169.
[4] J. Fienup *et al.*, "Aberration correction by maximizing generalized sharpness metrics," *JOSA A*, vol. 20, no. 4, pp. 609–620, 2003.
[5] M. I. Duersch *et al.*, "Backprojection autofocus for synthetic aperture radar," Ph.D. dissertation, Brigham Young University, 2013.
[6] D. E. Wahl *et al.*, "Phase gradient autofocus-a robust tool for high resolution SAR phase correction," *IEEE TAES*, vol. 30, no. 3, pp. 827–835, 1994.
[7] H. J. Callow *et al.*, "Stripmap phase gradient autofocus," in *IEEE OCEANS*, vol. 5, 2003, pp. 2414–2421.
[8] W. G. Carrera *et al.*, *Spotlight Synthetic Aperture Radar*. Artech House, Inc., 1995.
[9] C. Yang *et al.*, "Comparison of public peak detection algorithms for maldi mass spectrometry data analysis," *BMC Bioinformatics*, vol. 10, no. 1, p. 4, 2009.
[10] R. L. Morrison *et al.*, "Avoiding local minima in entropy-based sar autofocus," in *IEEE Workshop on SSP, 2003*, 2003, pp. 454–457.
[11] X. X. Zhu *et al.*, "Deep learning meets SAR," *to appear in IEEE GRS Maganize*, 2020.
[12] E. Mason *et al.*, "Deep learning for SAR image formation," in *Algorithms for Synthetic Aperture Radar Imagery XXIV*, vol. 10201. International Society for Optics and Photonics, 2017, p. 1020104.
[13] D. A. Cook *et al.*, "Analysis of phase error effects on stripmap SAS," *IEEE JOE*, vol. 34, no. 3, pp. 250–261, 2008.
[14] V. Badrinarayanan *et al.*, "Segnet: A deep convolutional encoder-decoder architecture for image segmentation," *IEEE PAMI*, vol. 39, no. 12, pp. 2481–2495, 2017.
[15] R. Zhang *et al.*, "The unreasonable effectiveness of deep features as a perceptual metric," in *IEEE CVPR*, 2018, pp. 586–595.
[16] C. Schlick, "Quantization techniques for visualization of high dynamic range pictures," in *Photorealistic rendering techniques*. Springer, 1995, pp. 7–20.
[17] T. J. Schulz, "Optimal sharpness function for SAR autofocus," *IEEE Signal Processing Letters*, vol. 14, no. 1, pp. 27–30, 2006.
[18] M. Abadi *et al.*, "TensorFlow: Large-scale machine learning on heterogeneous systems," 2015, software available from tensorflow.org. [Online]. Available: https://www.tensorflow.org/
[19] F. Gao *et al.*, "Implementing the nelder-mead simplex algorithm with adaptive parameters," *Computational Optimization and Applications*, vol. 51, no. 1, pp. 259–277, 2012.
[20] P. Getreuer, "Rudin-osher-fatemi total variation denoising using split bregman," *Image Processing On Line*, vol. 2, pp. 74–95, 2012.
[21] J. Bush, "Bregman algorithms," *Senior Thesis. University of California, Santa Barbara*, 2011.
[22] Z. Wang *et al.*, "Image quality assessment: from error visibility to structural similarity," *IEEE TIP*, vol. 13, no. 4, pp. 600–612, 2004.
[23] ——, "Multiscale structural similarity for image quality assessment," in *The Thrity-Seventh Asilomar Conference on Signals, Systems & Computers, 2003*, vol. 2, 2003, pp. 1398–1402.
[24] H. R. Sheikh *et al.*, "Image information and visual quality," *IEEE TIP*, vol. 15, no. 2, pp. 430–444, 2006.
[25] J. Zhou *et al.*, "A wavelet transform method to merge landsat tm and spot panchromatic data," *International Journal of Remote Sensing*, vol. 19, no. 4, pp. 743–757, 1998.
[26] L. Zhang *et al.*, "A comprehensive evaluation of full reference image quality assessment algorithms," in *IEEE ICIP*, 2012, pp. 1477–1480.
[27] D. C. Brown *et al.*, "A point-based scattering model for the incoherent component of the scattered field," *JASA*, vol. 141, no. 3, pp. EL210–EL215, 2017.
[28] D. P. Williams, "Exploiting phase information in synthetic aperture sonar images for target classification," in *IEEE OCEANS*, 2018, pp. 1–6.
[29] A. Hauptmann *et al.*, "On the unreasonable effectiveness of CNNs," *arXiv preprint arXiv:2007.14745*, 2020.
[30] T. Guo *et al.*, "Reinforced depth-aware deep learning for single image dehazing," in *IEEE ICASSP*, 2020, pp. 8891–8895.

Supplemental Materials: Deep Autofocus for Synthetic Aperture Sonar

Section I (S.I.) shows the top five defocused images with the best SSIM performance when compared to the benchmark images. We also show the estimated phase error correction of Deep Autofocus and the benchmark imagery. We see that the Deep Autofocus method accurately estimates the phase error even in scenes with complex backgrounds. Section II (S.II.) shows the top five defocused images with the worst SSIM performance when compared to the benchmark images. We see that Deep Autofocus is still performing well and that even the worst SSIM autofocused images are still quite good.

S.I. Top Five Defocused Images with Best SSIM

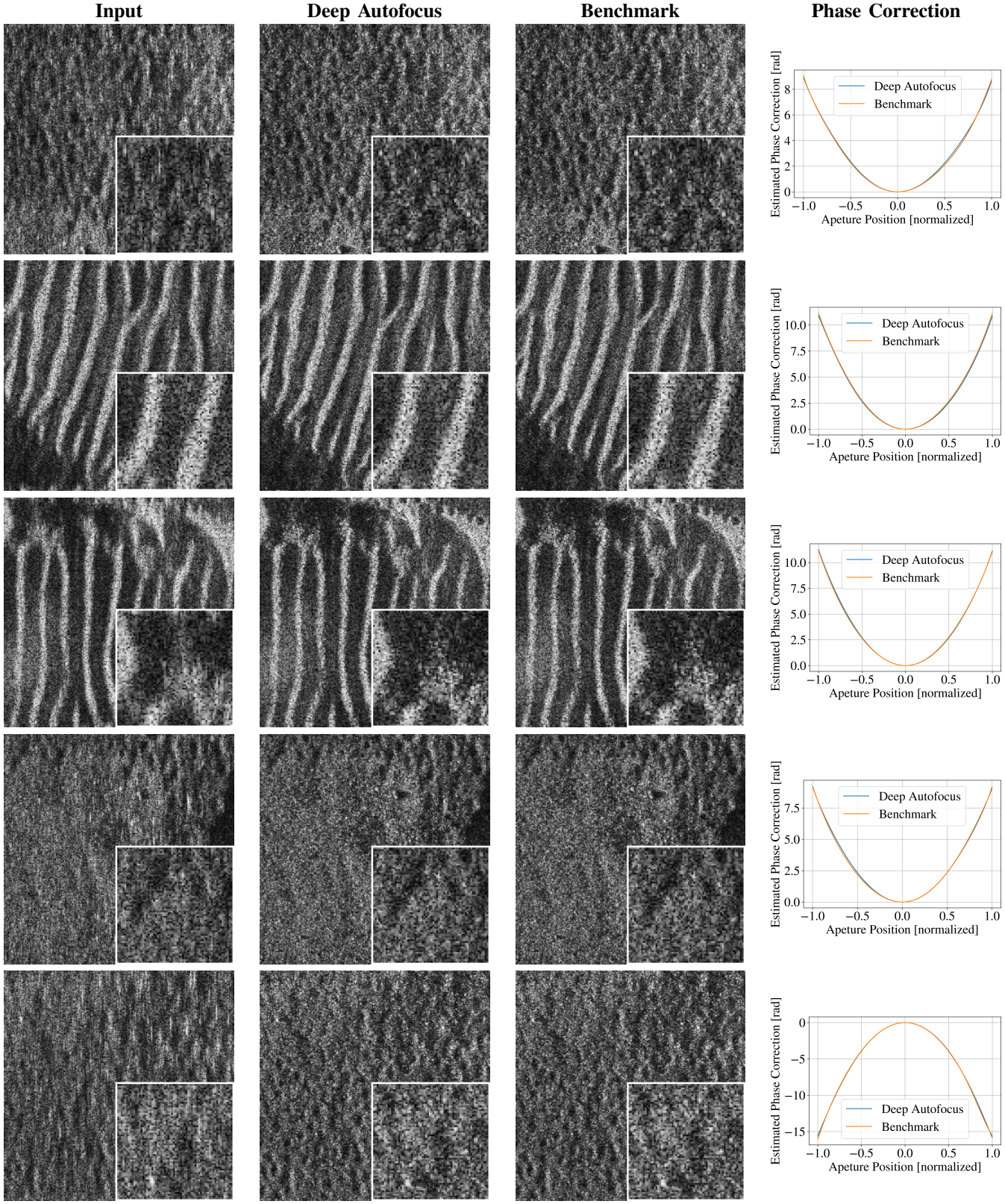

S.II. Top Five Defocused Images with Worst SSIM